InGaN diode pumped actively *Q*-switched intracavity frequency doubling $Pr:LiYF_4$ 261 nm laser

Junichiro Kojou, Ryo Abe, Ryosuke Kariyama, Hiroki Tanaka, Akira Sakurai, Yojiro Watanabe, and Fumihiko Kannari*

Department of Electronics and Electrical Engineering, Keio University, 3-14-1, Hiyoshi, Kohoku-ku, Yokohama 223-8522, Japan

*Corresponding author: kannari@elec.keio.ac.jp

Received 20 December 2013; revised 9 February 2014; accepted 15 February 2014; posted 18 February 2014 (Doc. ID 203378); published 25 March 2014

We demonstrate actively *Q*-switched deep ultraviolet laser operation at 261 and 320 nm by intracavity frequency doubling of an InGaN laser diode-pumped $Pr:LiYF_4$ laser. We obtain a maximum peak power of 61.6 W (8.7 μJ/pulse at 7.7 kHz) and 594 W (19.0 μJ/pulse at 7.7 kHz) with a pulse width of 142 and 35 ns at 261 and 320 nm, respectively. The conversion efficiency from the fundamental laser energy at 639 nm to the second-harmonic generation is 88%. Good agreement is obtained with prediction by a rate equation model.

OCIS codes: (140.7300) Visible lasers; (140.3610) Lasers, ultraviolet; (140.3580) Lasers, solid-state; (140.3515) Lasers, frequency doubled; (140.3540) Lasers, Q-switched.

http://dx.doi.org/10.1364/AO.53.002030

1. Introduction

Trivalent praseodymium (Pr^{3+})-doped materials have proven to be very promising laser sources due to their efficient stimulated emission in the visible region [1,2]. Laser action (red at 720, 697, and 639 nm; orange at 607 nm; green at 522 nm) has already been demonstrated with Pr^{3+}-doped fluoride crystals using InGaN diode lasers [3–6] as a pumping laser source. With advances in InGaN diode laser development, we can realize a high-power, compact all solid-state laser emitting in the visible spectral region. Another advantage of such visible lasers is that we can easily generate a coherent ultraviolet (UV) light by intracavity frequency doubling. Continuous-wave (cw) UV radiation at 261 and 320 nm has already been demonstrated by the intracavity second-harmonic generation (SHG) of $Pr:LiYF_4$ lasers operating at 522 and 639 nm, respectively [7–9], using high-power optically pumped semiconductor lasers as a pumping source. Recently, Gün *et al.* reported output power of 481 mW at 261 nm from an intracavity SHG of a $Pr:LiYF_4$ laser using two InGaN laser diodes whose maximum output power is ~1 W each [10].

The pulse laser oscillation of $Pr:LiYF_4$ was reported by Ruan *et al.* [11], who employed a 476 nm pump line of an Ar-ion laser and demonstrated passive mode-locking producing picosecond laser pulses (~10 ps) with a saturable absorber. Sutherland *et al.* demonstrated Kerr lens mode-locking with Ar-ion laser pumping and obtained 400 fs laser pulses at 613 nm [12]. Using an acousto-optic modulator (AOM), we reported a *Q*-switch operation at 639 nm and intracavity SHG [13]. Savitski *et al.* demonstrated passive *Q*-switching using a semiconductor saturable absorber mirror at 639 nm [14]. Very recently, we also achieved a passively *Q*-switched mode-lock operation using a thin Cr:YAG crystal as a saturable absorber at 639 nm [15]. Since, the stimulated emission cross section for the 522 nm transition is significantly smaller than that for 639 nm by a factor of ~7 [16], more intense pumping powers are required to achieve *Q*-switching.

1559-128X/14/102030-07$15.00/0

Employing a Pr^{3+}-doped fluoride glass fiber as the laser host, which can attain much higher small-signal gain than that in a $Pr:LiYF_4$ laser because of its smaller gain volume diameter, we demonstrated wavelength tunable active Q-switching in the visible region ranging from 488 to 491, 520 to 526, 601 to 624, and 631 to 644 nm [17].

In this paper, we extend the cw laser operation of a $Pr:LiYF_4$ laser at 522 and 639 nm to active Q-switching and an intracavity SHG for UV laser pulse generation.

2. Experiment

A. CW and Actively Q-switched Laser with a Straight Cavity

In our first experiment, we used a straight resonator with a 3.7 mm long $LiYF_4$ crystal doped with Pr^{3+} 0.5 at. %, which was cut parallel to the c axis. The crystal facets were polished for laser quality and remained uncoated. The pump beam was delivered by an InGaN laser diode (Nichia Co.) emitting around 444 nm. This 3.5 W diode laser's beam quality was $M^2 = 1.5 \times 12.9$ (fast axis × slow axis). This factor was estimated from its emitter size (1×30 μm) and its divergence angle ($2\theta = 45.9 \times 13.9$ deg). The pumping laser was collimated by a 4.6 mm focal length aspheric lens and shaped into a circular beam by a pair of cylindrical lenses with focal lengths of −20 and 100 mm, respectively. The pump beam was focused into the $Pr^{3+}:LiYF_4$ crystal by a 50 mm focal long focusing lens. The laser cavity consisted of a flat dichroic pumping mirror and a concave output mirror ($R = 75$ mm). The laser crystal was placed near the pumping mirror to improve the matching between the pumping volume and the fundamental resonator mode. The transverse modes of the fundamental resonator mode and the pump beam were calculated by the ABCD matrix method [18]. For a cavity length of 75 mm, fundamental resonator mode radii were obtained as 36.1 and 40.0 μm, and the mode matching efficiency was estimated to 83.8 and 85.1% for lasing wavelengths of 522 and 639 nm, respectively, without a thermal lens in the laser crystal. For stable laser operation, the laser crystal must be cooled by a Peltier device and an air cooling fan. In fact, from our numerical calculation, since a strong thermal lens of a negative focal length of −13 mm was formed at an absorbed pump power of 2.3 W, our resonator could no longer satisfy the condition for a stable cavity.

When the laser diode was operated without particular temperature control (a conventional Peltier device and air cooling preventing thermal damage to the laser diode was supplied), the emission wavelength shifted from 443 to 445 nm as the current increased from 300 mA to 2.3 A. Therefore, to get an optimal wavelength for pumping the $Pr:LiYF_4$ crystal, at the highest injection current of 2.3 A, the laser diode temperature was kept at 5°C. The laser crystal was oriented for maximum pumping power absorption with the c axis parallel to the electric field vector of the linearly polarized pump laser. The optimum pumping wavelength at π-polarization was found at 444 nm. The oscillations at 522 and 639 nm were σ and π, respectively.

For the Q-switch operation, an AOM (Fused Silica, GOOCH & HOUSEGO UL Ltd.) was inserted into the cavity, which is operated by RF frequency at 200 MHz. Both sides of the AOM were antireflection (AR) coated for the visible region. The highest diffraction efficiency of this AOM was 70%. Its optical loss was ~3% at 522 and 639 nm.

B. Actively Q-switched Laser and SHG with a V-shaped Cavity (320 nm)

For an intracavity SHG at 320 nm, we employed a V-shaped cavity setup (Fig. 1) with two laser mode waists. Plane mirror M3 is highly reflective (HR) coated (>99.7%) at both 639 and 320 nm. Mirrors M1 and M2 are HR coated (>99.7%) for 639 nm. The M1 mirror is highly transparent (>90%) at 444 nm. The M2 mirror with a 75 mm curvature radius is highly transparent (>90%) at 320 nm. Thus, we measured the 320 nm power from the M2. In the absence of the nonlinear crystal the 639 nm radiation was coupled out of the cavity by means of a 1.5 mm thick-fused silica plate placed between mirrors M2 and M3 with an appropriate angle to maximize the extracted laser power. The diode laser emitting up to 3.5 W at 445 nm was focused into the crystal with π-polarization. The lens with a focal length of 50 mm was used to focus the pump beam into the laser crystal. The highest absorption power achieved by this arrangement was 2.4 W. The spot size of the fundamental resonator mode was 58.0 μm × 37.0 μm under no thermal lens formation in the laser crystal. The mode matching efficiency was 81.4%. The V-shaped cavity provides a slightly elliptical beam waist of about a 45.0 μm × 33.5 μm radius in the nonlinear crystal. For an intracavity SHG, an 8 mm long, LBO (LiB_3O_5) type I crystal ($\phi = 53.6°$) was used. Both of its sides were AR coated for 639 nm.

C. Actively Q-switched Laser and SHG with a V-shaped Cavity (261 nm)

For an intracavity SHG at 261 nm, the V-shaped cavity setup is almost the same as that used for

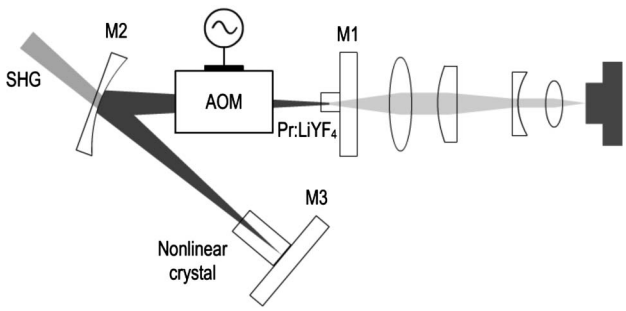

Fig. 1. Schematic view of V-shaped laser cavity for intracavity SHG of an actively Q-switched $Pr:LiYF_4$ laser pumped by InGaN diode laser.

the 320 nm SHG (Fig. 1). Plane mirror M3 was HR coated at both 522 (>99%) and 261 nm (>97%). The mode matching efficiency was 79.7%. Mirrors M1 and M2 were HR coated (>99.5%) for 522 nm. The spot size of the fundamental resonator mode was 51.0 μm × 32.5 μm under no thermal lens formation at the laser crystal. The M1 was highly transparent (>90%) at 444 nm. The M2 output mirror with a 75 mm curvature radius was highly transparent (>70%) at 261 nm. The V-shaped cavity provides a slightly elliptical beam waist of about 41.0 μm × 34.5 μm radius in the nonlinear crystal. For an intracavity SHG, a 7 mm long β-BaB_2O_4 (BBO) type I crystal ($\phi = 48.9°$) was used. Both of its sides were AR coated for 522 nm.

3. Results and Discussion

A. CW Laser with a Straight Cavity

Figure 2 shows the output power of two different laser wavelengths, 522 and 639 nm, as a function of the Pr:$LiYF_4$ crystal's absorbed pumping laser power, which was obtained at a nonlasing condition from the launched and transmitted pumping laser powers. The wavelength of the InGaN diode laser exhibits redshift as the injection current increases and the absorption coefficient of the laser crystal changes. We cannot therefore evaluate accurately whether pumping laser absorption exhibits saturation at higher pumping laser powers due to depletion of Pr^{3+} ions in the ground state [19]. If the pumping is saturated, the absorbed pumping laser power estimated under nonlasing conditions will be lower than the actual value at the lasing condition since the upper laser level population is clamped at the lasing threshold. Therefore, we measured the transmitted pumping laser power through the Pr:$LiYF_4$ crystal under the lasing condition and compared it with the nonlasing condition. We found no difference between the transmitted laser powers at the lasing and nonlasing conditions up to a launched InGaN laser power of 500 mW. The transmitted power at the lasing condition became slightly higher than that at the nonlasing condition. We measured the excess absorption power of only 24 mW at a launched InGaN laser power of 2.44 W. In the range of our pumping power density, we can use the pumping laser power absorbed at the nonlasing condition to calculate the laser slope efficiency.

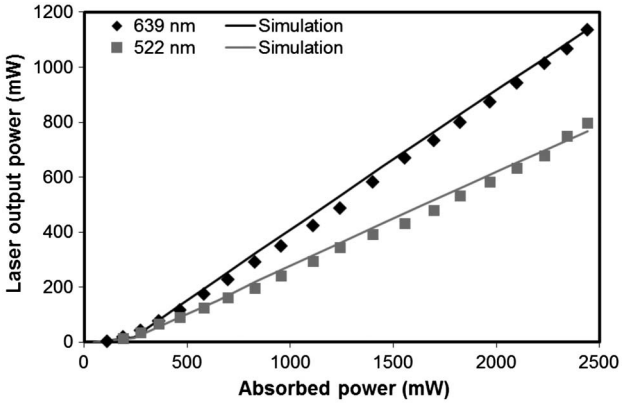

Fig. 2. Plots of cw laser output power obtained from a straight cavity as function of absorbed pumping laser power for 522 and 639 nm. Diamonds stand for experimental results at 639 nm and squares at 522 nm. Straight lines are numerical simulation results from rate equations.

As shown in Fig. 2, the laser power increases linearly with our estimated absorbed laser power. The threshold pump power was 208 mW. The slope efficiency with respect to the absorbed pumping laser power was 34%. 797 mW of the green cw laser was obtained for absorbed pump power of 2.44 W. At 639 nm, the best performance was achieved with an output coupling of $T = 10\%$. The threshold pump power was 237 mW. The slope efficiency with respect to the absorbed pumping laser power was 50%. 1.14 W of the red cw laser was obtained for absorbed pump power of 2.44 W. This laser is well described by the following conventional rate equations [20]:

$$\frac{dN_g}{dt} = -\frac{N_g}{N_{g0}}\frac{\eta_p\eta_q\eta_m P_{\text{in}}}{h\nu_L V} + \frac{N_l}{\tau_l}, \tag{1}$$

$$\frac{dN_l}{dt} = \left(c\sigma_{\text{st}}\phi + \frac{1}{\tau_f}\right)N_u - \frac{N_l}{\tau_l}, \tag{2}$$

$$\frac{dN_u}{dt} = \left(-c\sigma_{\text{st}}\phi - \frac{1}{\tau_f}\right)N_u + \frac{N_g}{N_{g0}}\frac{\eta_p\eta_q\eta_m P_{\text{in}}}{h\nu_L V}, \tag{3}$$

$$\frac{d\phi}{dt} = \left\{\frac{c\sigma_{\text{st}}l}{l_c}(N_u - N_l) - \frac{c}{2l_c}\left(\ln\left(\frac{1}{R_1R_2}\right) + L_i\right)\right\}\phi + \frac{\xi N_u}{\tau_f}, \tag{4}$$

$$P_{\text{out}} = -\frac{1}{2}\ln(R_1R_2)Ah\nu_L c\phi, \tag{5}$$

where P_{in} is the absorbed pump power; N_g is the population density of the ground state and N_{g0} is its initial value; N_u and N_l are the population densities of the upper and the lower laser levels, respectively; η_p is the pumping efficiency; η_q is the quantum efficiency; η_m is the mode-matching efficiency; h is Planck's constant; c is the speed of light; V is the mode volume; ν_L is the frequency of the laser oscillation; τ_l is the lifetime of the lower laser level; τ_f is the fluorescence lifetime; σ_{st} is the stimulated emission cross section; ϕ is the photon density in the cavity; l is the laser crystal length; l_c is the cavity length; R_1 and R_2 are the reflectivity of the plane and concave mirrors, respectively; ξ is the contribution of spontaneous emission; A is the mode cross section, and L_i is the cavity round-trip loss. In our simulation, cavity round-trip loss L_i is a fitting parameter. We solved these rate equations. As mentioned before,

without cooling the laser crystal, our resonator could no longer satisfy the condition for a stable cavity with high pump power due to the formation of a strongly negative thermal lens. By theoretical calculation of the thermal lens [20], its focal lengths were predicted as −15.3(⊥) and −12.3 mm(∥) for 2.44 W pump power absorption. In our setup, the laser crystal was cooled to attenuate the thermal lens effect. Consequently, the focal length of the thermal lens was estimated as −80 mm from the numerical simulations. The temperature control roughly reduced the thermal effect by a factor of 6. The M^2 factor of the InGaN diode laser was measured for different pump powers (Fig. 3). Around the oscillation threshold of the laser diode, the M^2 factor was estimated as 1.1 × 9.3, and for high-power pumping (injection current of 2.3 A), the factor increased up to 1.5 × 12.9.

Simultaneously the mode-matching efficiency changed with the pumping power. When it was 500 mW, the mode-matching efficiency was calculated as 92.5%, and with a maximum pump power of 2.44 W, it decreased to 83.8%. This change of the mode-matching efficiency due to the variance of the M^2 factor was considered in our simulation as well as the mode-matching efficiency modified by the thermal lens formation (Fig. 3).

Consequently, the numerical results coincided with the experimental results with a cavity round-trip loss of 1.6 and 1.0% at 522 and 639 nm, respectively. Gün *et al.* achieved a slope efficiency of 61% (64%) and a maximum output power of 760 mW (877 mW) with an absorbed power of 1.44 W for 522 nm (639 nm) [6]. They used an output coupler of 1.28% (2.46%) transmittance and estimated the internal cavity loss as 0.49% (0.23%) [6]. Our slope efficiency was lower than their results. This is because the internal cavity loss of 1.6% in our experiment was much larger than their result, presumably due to the laser crystal quality. In fact, we tested several laser crystals grown by different manufacturers. Even if the length and the doping concentration were the same, the laser performance was quite different, presumably due to the residual loss. Moreover, since Gün *et al.* employed a shorter laser crystal (2.9 mm long), the mode-matching efficiency was higher than that of our experiment.

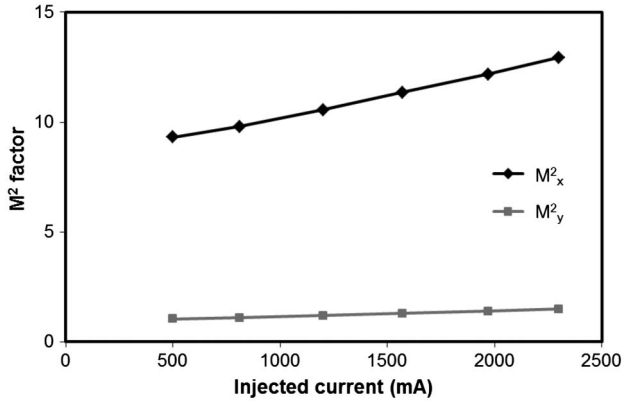

Fig. 3. Plots of mode-matching efficiency and M^2 factor as functions of absorbed pumping laser power.

B. Actively *Q*-switched Laser with a Straight Cavity

Figure 4 shows the output peak power and the pulse width (FWHM) of the *Q*-switched laser at 522 nm as a function of initial inversion ratio r, which is defined as the absorbed pumping laser power divided by the threshold power (380 mW). The residual loss of the AOM was 3%. The output coupling was 2%. Three different *Q*-switching sequences were compared. The laser extraction time window was set at 10 μs, which is much longer than the resultant *Q*-switched laser pulse width. We shortened this window and increased the average output power. Cavity *Q* was kept at a minimum for 40, 80, or 120 μs by applying the RF signal to the AOM since the radiative lifetime of the lasing upper state is 38 μs. The highest laser peak power of 102 W (3.3 μJ/pulse, 7.7 kHz) and the pulse width of 32 ns were obtained at $r = 6.4$.

We calculated the pulse peak power and the *Q*-switched pulse width by the rate equation model. The *Q*-switched laser can be predicted by Eqs. (1)–(4) and the following equation of the photon density:

$$\frac{d\phi}{dt} = \left\{\frac{c\sigma_{\mathrm{st}} l}{l_c}(N_u - N_l) - \frac{c}{2l_c}\left(\ln\left(\frac{1}{R_1R_2}\right) + L_i + L_{\mathrm{AOM}}(t)\right)\right\}\phi + \frac{\xi N_u}{\tau_f}, \quad (6)$$

where $L_{\mathrm{AOM}}(t)$ is the diffraction efficiency of the AOM. Equation (4) was modified to Eq. (6) by adding the loss due to AOM. We solved these rate equations for two different losses of the AOM. For its on-time and off-time, the internal cavity loss was 44.5% and 4.5%, respectively. The calculated results using Eqs. (1)–(3), (5), and (6) showed good agreement with the changes in the laser pulse widths shown in Fig. 4.

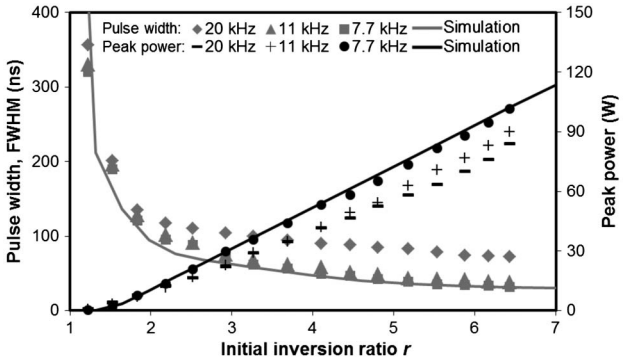

Fig. 4. Plots of *Q*-switched 522 nm laser peak power and pulse width obtained from a straight cavity as functions of the initial inversion ratio r, defined by absorbed pumping laser power divided by threshold pumping power (= 380 mW). Output coupling T is 2%. At repetition rate of 20 kHz, AOM was switched on for 10 μs and switched off for 40 μs. At 11 kHz and 7.7 kHz, AOM was switched on for 10 μs and switched off for 80 and 120 μs, respectively. Solid curves stand for pulse width and peak power obtained from simulation.

At $r = 6.4$, the extraction efficiency reached 40%, and a pulse width of 30 ns was obtained. Even if the pumping power were increased to $r > 10$, the pulse width would not be shorter than 20 ns. Taking into account the change of the M^2 factor of the pump beam and the mode-matching efficiency as the pump power increases, the calculation results fit the experimental results well.

We repeated the same Q-switching experiment for a laser wavelength of 639 nm and obtained the highest peak power of 1.57 kW (27 μJ/pulse) and a 17 ns pulse width at a repetition rate of 7.7 kHz at $r = 18.1$.

C. Actively Q-switched Laser and SHG with a V-shaped Cavity

Compared with a straight cavity, the V-shaped cavity shows slightly higher lasing threshold for lasing at 522 and 639 nm. At 522 nm, the highest peak power of 92 W (12.9 μJ/pulse, pulse with of 140 ns) was obtained at a repetition rate of 7.7 kHz without a BBO nonlinear crystal. Compared with the straight cavity, the pulse width became much longer owing to the lower initial inversion ration r. In addition, during the experiment of 522 nm Q-switching with the straight cavity, we adjusted the cavity so that the highest peak power was obtained. Since sufficiently higher initial inversion ratios were secured, a slightly lossy cavity generated the shortest pulse width at a cost of laser output energy, where consequently the peak laser power was highest. With the V-shaped cavity, we adjusted the cavity so that the highest output energy was obtained. In fact, since the initial inversion ratio was lower, this adjustment manner also generated the highest peak power. Consequently, the highest laser peak power obtained with the V-shaped cavity was slightly lower than that obtained with the straight cavity.

Figure 5 shows the change in the output peak power and the pulse width (FWHM) of the intracavity SHG pulse as a function of r, where the threshold power was 730 mW. The highest peak power of 62 W (8.7 μJ/pulse, average power of 67 mW) and a pulse width of 142 ns were obtained at 261 nm at a repetition rate of 7.7 kHz and $r = 3.3$. Thus, the conversion efficiency from extracted fundamental laser energy 12.9 μJ to second-harmonic (SH) pulse energy 8.7 μJ was ~68%. The BBO crystal induces a more significant walk-off effect than the LBO crystal. The walk-off angles are 86.5 and 18.5 mrad for BBO and LBO, respectively. Consequently, the SH beam split into two different directions using the BBO crystal. In fact, we can compensate this walk-off effect by inserting a second BBO crystal in the symmetric configuration. In our experiments, only one BBO crystal was employed. Figure 6 shows the observed oscilloscope traces of the SH laser pulse at an output peak power of 61.6 W. For this measurement, a biplanar photo tube (Hamamatsu Photonics, R1328U-04) was employed. The pulse train is presented in Fig. 6, indicating that the repetition rate was 7.7 kHz. A single SH pulse envelope with a laser pulse width of 142 ns is shown in Fig. 7.

The pulse peak power and the SH pulse width were calculated by Eqs. (7) and (8). The last term of Eq. (7) shows that a portion of the fundamental wave was converted to an SH wave. Here, γ is the SHG

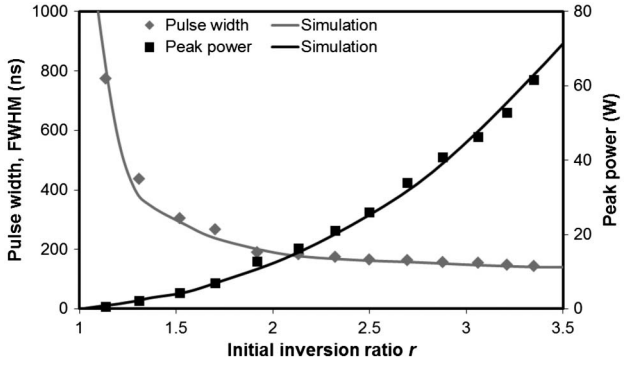

Fig. 5. Plots of SH laser peak power and pulse width at 261 nm obtained from V-shaped cavity as functions of initial inversion ratio r. Threshold pumping power is 730 mW. Pulse repetition rate is 7.7 kHz. Solid lines stand for pulse width and peak power obtained from simulation.

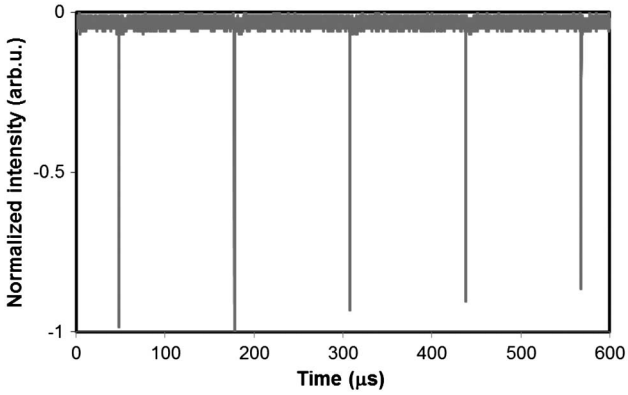

Fig. 6. Observed oscilloscope trace of pulse train (measured with a biplanar photo tube) of SH pulse at 261 nm.

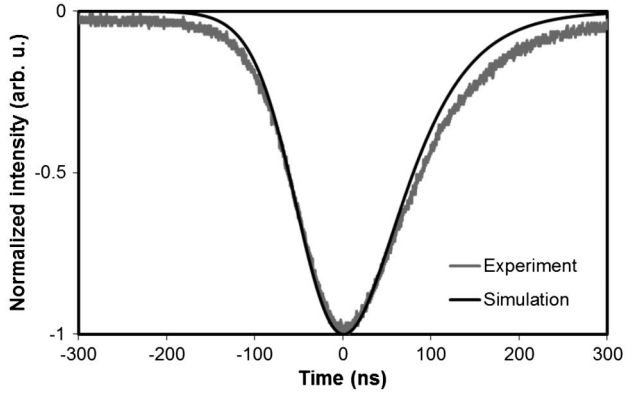

Fig. 7. 261 nm SH pulse envelope (measured with a biplanar photo tube) at output peak power of 61.6 W. The solid curve stands for the simulation pulse shape.

coefficient; A_ω and $A_{2\omega}$ are the beam cross sections of the fundamental and SH wavelengths in the nonlinear crystal, respectively; ε is the area ratio of the fundamental wavelength mode area and the SH beam area; and $P_{2\omega}$ is the peak power of the SH pulse [10]:

$$\frac{d\phi}{dt} = \left\{\frac{c\sigma_{\mathrm{st}} l}{l_c}(N_u - N_l) - \frac{c}{2l_c}\left(\ln\left(\frac{1}{R_1 R_2}\right) + L_i + L_{\mathrm{AOM}}(t)\right)\right\}\phi + \frac{\xi N_u}{\tau_f} - \frac{c}{2l_c}(2c\gamma h\nu_\omega A_\omega \varepsilon\phi)\phi, \quad (7)$$

$$P_{2\omega} = \frac{c}{l_c}(2c\gamma h\nu_\omega A_\omega \varepsilon\phi)\phi T_{2\omega} l_c A_\phi h\nu_\omega. \quad (8)$$

For the AOM's off-time, the cavity round-trip loss was evaluated as 5%. We solved these rate equations considering SHG coefficient γ as a fitting parameter, which was finally estimated as 5.0×10^{-5}/W. Gün *et al.* [10] demonstrated an intracavity cw SHG at 261 nm and estimated SHG coefficient γ as 4.0×10^{-5}/W. We realized good fitting of the numerical simulation results to the experimental results, taking into account the change of the mode-matching efficiency for different pump power.

At 639 nm, we obtained the highest Q-switched output energy of 21.7 μJ at a repetition rate of 7.7 kHz without the LBO nonlinear crystal. The fundamental wavelength's output power was extracted by placing a fused silica plate in the cavity. The pulse width of the 639 nm pulse was 32 ns, which is longer than the shortest pulse width of 17 ns obtained by the straight cavity. Since the initial inversion ratio is still sufficiently high, the pulse width did not increase so much, which is a large difference from the 522 nm pulse in the V-shaped cavity. Figure 8 shows the change in the output peak power and the pulse width (FWHM) of the intracavity SH pulse as a function of r, where the threshold power was 364 mW. A highest peak power of 594 W (19.0 μJ/pulse, average power of 380 mW) and a pulse width of 35 ns were obtained at 320 nm at a repetition rate of 7.7 kHz and $r = 6.7$. Thus the conversion efficiency from extracted fundamental laser energy of 21.7 μJ to SH pulse energy of 19.0 μJ was ~88%. For the AOM's off-time, the cavity round-trip loss was estimated as 5%, and SHG coefficient γ, as the fitting parameter, was finally estimated as 6.0×10^{-5}/W. Zhou *et al.* [21] demonstrated an intracavity cw SHG at 400 nm and estimated SHG coefficient γ as 2.04×10^{-5}/W. The type I SHG properties of BBO for 522 nm and LBO for 639 nm are summarized in Table. 1.

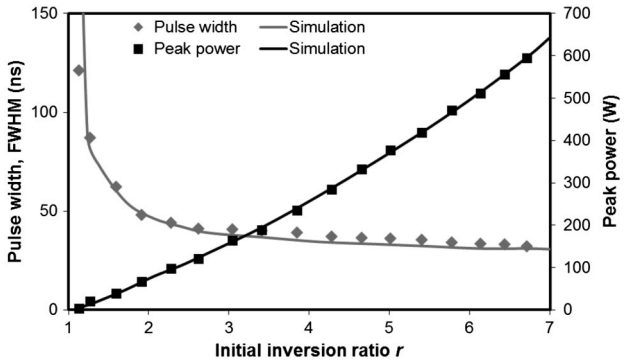

Fig. 8. Plots of SH laser peak power and pulse width at 320 nm obtained from V-shaped cavity as function of initial inversion ratio r. Threshold pumping power is 364 mW. Pulse repetition rate is 7.7 kHz. The solid curves stand for pulse width and peak power obtained from simulation.

4. Conclusions

We demonstrated actively Q-switched deep UV laser operation at 261 and 320 nm by intracavity frequency doubling of an InGaN laser diode pumped $Pr:LiYF_4$ laser. Numerical analyses using rate equations agreed well with these experimental results.

For 522 nm lasing, we achieved cw output power of 797 mW and obtained a maximum peak power of 102 W (3.3 μJ/pulse) with a pulse width of 32 ns at a 7.7 kHz repetition frequency. From an actively Q-switched $Pr:LiYF_4$ laser, employing a BBO as an SHG nonlinear crystal in the V-shaped cavity, we obtained a maximum peak power of 61.6 W (8.7 μJ/pulse) at 261 nm with a pulse width of 142 ns. Although the optical loss of our HR mirrors at the fundamental wavelength was relatively high at ~2%, higher intracavity wavelength conversion efficiency was obtained by the Q-switching operation. The conversion efficiency from extracted fundamental laser energy of 12.9 μJ to SH pulse energy of 8.7 μJ was ~68%.

For 639 nm lasing, we obtained a maximum peak power of 594 W (19.0 μJ/pulse) at 320 nm with a pulse width of 35 ns from an actively Q-switched $Pr:LiYF_4$ crystal in a V-shaped cavity with the LBO as a SHG nonlinear crystal. The conversion efficiency from extracted fundamental laser energy of 21.7 μJ to SH pulse energy of 19.0 μJ was ~88%.

Table 1. Comparison of BBO and LBO Type I SHG Properties

Wavelength (nm)	Crystal	Phase-Matching Angle (deg)	Walk-off (deg)	SHG Coefficient ($\times 10^{-5}$/W)	Total Loss L_i + AOM + Crystal (%)
522	BBO	48.9	3.10	5	5.00
639	LBO	53.6	1.06	6	4.50

References

1. R. G. Smart, J. N. Carter, A. C. Tropper, and D. C. Hanna, "CW room temperature operation of praseodymium-doped fluorozirconate glass fibre lasers in the blue-green, green and red spectral regions," Opt. Commun. **86**, 333–340 (1991).
2. T. Sandrock, T. Danger, E. Heumann, G. Huber, and B. H. T. Chai, "Efficient continuous wave-laser emission of Pr^{3+}-doped fluorides at room temperature," Appl. Phys. B **58**, 149–151 (1994).
3. A. Richter, E. Heumann, E. Osiac, G. Huber, W. Seelert, and A. Diening, "Diode pumping of a continuous-wave Pr^{3+} doped $LiYF_4$ laser," Opt. Lett. **29**, 2638–2640 (2004).
4. K. Hashimoto and F. Kannari, "High-power GaN diode-pumped continuous wave Pr^{3+}-doped $LiYF_4$ laser," Opt. Lett. **32**, 2493–2495 (2007).
5. N.-O. Hansen, A.-R. Bellancourt, U. Weichmann, and G. Huber, "Efficient green continuous-wave lasing of blue-diode-pumped solid-state lasers based on praseodymium-doped $LiYF_4$," Appl. Opt. **49**, 3864–3868 (2010).
6. T. Gün, P. Metz, and G. Huber, "Power scaling of laser diode pumped Pr^{3+}:$LiYF_{4\ cw}$ lasers: efficient laser operation at 522.6 nm, 545.9 nm, 607.2 nm, and 639.5 nm," Opt. Lett. **36**, 1002–1004 (2011).
7. A. Richter, N. Pavel, E. Heumann, G. Huber, D. Parisi, A. Toncelli, M. Tonelli, A. Diening, and W. Seelert, "Continuous-wave ultraviolet generation at 320 nm by intracavity frequency doubling of red-emitting praseodymium lasers," Opt. Express **14**, 3282–3287 (2006).
8. V. Ostroumov, W. Seelert, and L. Hunziker, "522/261 nm cw generation of Pr:YLF laser pumped by OPS laser," Proc. SPIE **6451**, 645104 (2007).
9. V. Ostroumov, W. Seelert, L. Hunziker, A. Richter, E. Heumann, and G. Huber, "UV generation by intracavity frequency doubling of an OPS-pumped Pr:YLF laser with 500 mW of cw power at 360 nm," Proc. SPIE **6451**, 645103 (2007).
10. T. Gün, P. Metz, and G. Huber, "Efficient continuous wave deep ultraviolet Pr^{3+}: $LiYF_4$ laser at 261.3 nm," Appl. Phys. Lett. **99**, 181103 (2011).
11. S. Ruan, J. M. Sutherland, P. M. W. French, and J. R. Taylor, "Kerr-lens mode-locked visible transitions of a Pr:YLF laser," Opt. Lett. **20**, 1041–1043 (1995).
12. J. M. Sutherland, B. H. T. Chai, P. M. W. French, and J. R. Taylor, "Visible continuous-wave laser transitions in Pr^{3+}:YLF and femtosecond pulse generation," Opt. Lett. **21**, 797–799 (1996).
13. J. Kojou, Y. Watanabe, Y. Kojima, H. Nemoto, and F. Kannari, "Intra-cavity second-harmonic generation at 320 nm of an actively *Q*-switched Pr:LiYF4 laser," Appl. Opt. **51**, 1382–1386 (2012).
14. V. G. Savitski, I. M. Ranieri, A. B. Krysa, and S. Calvez, "Passively *Q*-switched Pr:YLF laser," in *Conference on Laser and Electro-Optics (CLEO 2011)*, OSA Technical Digest (CD) (Optical Society of America, 2011), paper CMB7.
15. R. Abe, J. Kojou, K. Masuda, and F. Kannari, "Cr^{4+}-doped $Y_3Al_5O_{12}$ as a saturable absorber for a *Q*-switched and mode-locked 639-nm Pr^{3+}-doped $LiYF_4$ laser," Appl. Phys. Express **6**, 032703 (2013).
16. G. Huber, A. Richter, and E. Heumann, "Continuous wave praseodymium solid-state lasers," Proc. SPIE **6451**, 645102 (2007).
17. J. Kojou, Y. Watanabe, P. Agrawal, T. Kamimura, and F. Kannari, "Wavelength tunable *Q*-switch laser in visible region with Pr^{3+}-doped fluoride-glass fiber pumped by GaN diode laser," Opt. Commun. **290**, 136–140 (2013).
18. H. Kogelnik and T. Li, "Laser beams and resonators," Appl. Opt. **5**, 1550–1567 (1966).
19. Y. Sato and T. Taira, "Saturation factors of pump absorption in solid-state lasers," IEEE J. Quantum Electron. **40**, 270–280 (2004).
20. W. Koechner, *Solid-State Laser Engineering* (Springer-Verlag, 1988).
21. W.-L. Zhou, Y. Mori, T. Sasaki, and S. Nakai, "High-efficiency intracavity continuous-wave ultraviolet generation using crystals CsLiB6010, β-BaB_2O_4, and LiB_30_5," Opt. Commun. **123**, 583–586 (1996).